

Measuring high field gradients of cobalt nanomagnets in a spin-mechanical setup

Cite as: Appl. Phys. Lett. **128**, 054001 (2026); doi: [10.1063/5.0301921](https://doi.org/10.1063/5.0301921)

Submitted: 11 September 2025 · Accepted: 19 December 2025 ·

Published Online: 3 February 2026










View Online



Export Citation



CrossMark

Felix Hahne,^{1,2}  Teresa Klara Pfau,^{1,2}  Liza Žaper,³  Lucio Stefan,^{1,2}  Thibault Capelle,^{1,2} 
 Andrea Ranfagni,^{1,2}  Martino Poggio,^{3,4}  and Albert Schliesser^{1,2,a)} 

AFFILIATIONS

¹Niels Bohr Institute, University of Copenhagen, Blegdamsvej 17, 2100 Copenhagen, Denmark

²Center for Hybrid Quantum Networks, Niels Bohr Institute, University of Copenhagen, Blegdamsvej 17, 2100 Copenhagen, Denmark

³Department of Physics, University of Basel, 4056 Basel, Switzerland

⁴Swiss Nanoscience Institute, University of Basel, 4056 Basel, Switzerland

^{a)} Author to whom correspondence should be addressed: albert.schliesser@nbi.dk

ABSTRACT

Hybrid systems composed of a single nitrogen-vacancy center spin magnetically coupled to a macroscopic mechanical resonator constitute promising platforms for the realization of quantum information protocols and for quantum sensing applications. The magnetic structure that mediates the interaction must ensure high field gradients while preserving the spin and mechanical properties. We present a spin-mechanical setup built around a cobalt nanomagnet grown with focused electron beam-induced deposition. The magnetic structure is fully characterized, and a maximum gradient of 170 kT m^{-1} is directly measured at a spin-oscillator distance of a few hundred nanometers. Spin coherence was preserved at the value of $20 \mu\text{s}$ up to a gradient of 25 kT m^{-1} . The effect of the mechanical motion on the spin dynamics was observed, thus signifying the presence of spin-mechanics coupling. Given the noninvasive nature of the nanomagnet deposition process, we foresee the adoption of such structures in hybrid platforms with high-quality factor resonators, in the “magnet on oscillator” configuration.

Published under an exclusive license by AIP Publishing. <https://doi.org/10.1063/5.0301921>

Following the landmark experiment¹ that revealed how a single electron spin can exert a measurable force on a macroscopic cantilever, various hybrid platforms composed of two-level systems coupled to macroscopic oscillators have emerged by integrating mechanical resonators with superconducting qubits^{2–5} and solidstate defects.^{6,7} Thanks to the mature technology of ultra-high-quality factor oscillators,⁸ these platforms are appealing as testbeds for quantum information processing experiments⁹ and also for pushing the boundaries of quantum sensing.¹⁰

The paradigmatic system of a single spin coupled to a mechanical resonator device has been successfully implemented using nitrogen-vacancy (NV) defects in diamond¹¹ coupled to the mechanics via strain^{12,13} or magnetically.^{14–20}

When a magnetically decorated oscillator is placed in the vicinity of an NV center,²¹ the Zeeman interaction results in a parametric single-phonon coupling strength $g_0 = 2\pi\gamma_{\text{NV}}G_z z_{\text{zpf}}$, where $\gamma_{\text{NV}} \simeq 28 \text{ GHz T}^{-1}$ is the gyromagnetic ratio of the NV center, $G_z = \partial B_{\text{NV}} / \partial z$ is the gradient at the NV rest position—along the oscillator’s motion direction (z)—of the magnetic field component (B_{NV}) parallel to the NV spin quantization axis, and $z_{\text{zpf}} = \sqrt{\hbar/2m\Omega_m}$ is the zero-point

motion amplitude, where \hbar is the reduced Planck constant, Ω_m is the oscillator’s angular frequency, and m is its mass.

A crucial requirement for implementing quantum protocols is achieving a quantum cooperativity greater than one, with the cooperativity defined¹⁵ as $C = g_0^2 T_2 \Gamma^{-1}$, where Γ is the decoherence rate of the oscillator and T_2 denotes the spin transverse relaxation time under a specific decoupling sequence. When $C > 1$, the zero-point mechanical fluctuations could be resolved within a few shot measurements.^{15,22} In this regime, a hot mechanical resonator could be exploited to realize quantum gates between two spins in a hybrid nano-electromechanical system,²³ or—when $C > 4$ —to efficiently generate entanglement between two spin qubits.²⁴

An important challenge currently faced by the community in this regard is the research of a suitable magnetic structure, which must achieve high magnetic field gradients while preserving both the oscillator’s properties and the overall system coherence.²⁵ Different methods have been explored, including the use of NdFeB magnetic structures,¹⁴ a CoFe magnetic film evaporated onto a quartz tip,¹⁹ a CoCr layer deposited on a tip,¹⁵ and NdFeB beads.^{16,18}

Here, we harness the nanometric control of focused electron beam-induced deposition (FEBID)²⁶ to grow soft cobalt nanomagnets on a silicon chip. The nanomagnetic structure, which exhibits strong magnetic gradients, is installed in a spin-mechanics setup based on a scanning NV microscopy configuration.

The scanning NV microscopy configuration we use for this work utilizes x , y , and z piezoelectric nanopositioners (attocube), allowing nanometer-resolution spatial positioning of the mounted tuning fork with the NV center relative to a selected sample with the nanomagnets [Fig. 1(a)]. The nanomagnets are magnetized by a homogeneous external magnetic bias field of up to 140 mT generated by a spherical magnet, which is aligned to the NV quantization axis. We use a cost-efficient semiconductor laser (Cobolt 06-01 Series) with 515 nm wavelength that efficiently excites the NV center, and collect the resulting photoluminescence with a home-built confocal microscope with a 0.9 NA objective (Olympus MPlanFL N 100x). The scanning system is configured vertically to allow the insertion of a permanent magnet for magnetic biasing on the back side of the sample chip.

The core of the system consists of a 100-cut diamond scanning probe (QZabre QST²⁷) hosting the NV center and a Si chip with the Co nanomagnets plus an integrated microwave stripline for spin control [Fig. 1(b)]. The nanomagnet of this study is approximately 40 μm away from the stripline and has a cylindrical shape with 830 nm height and 400 nm diameter.

To grow these nanomagnets, we employ FEBID with the geometry defined as a circular pattern and the following parameters: an acceleration voltage of 5 kV, a beam current of 100 pA, a dwell time of 1 μs , and a precursor flux corresponding to a vacuum pressure varying in the range 1.1×10^{-6} mbar to 1.2×10^{-6} mbar (see [supplementary material S1.2](#)).

We perform magnetometry measurements^{28–30} to characterize the stray field $\mathbf{B}_{\text{nm}}(x, y, z)$ emanating from the nanomagnet. We measure the shift in the lower energy electron spin resonance of the optical ground state spin triplet while performing a xy raster scans on planes above the magnetic structure. The optically detected magnetic resonance (ODMR) is performed at each position (x, y) by applying a continuous-wave microwave sweep and acquiring the NV center photoluminescence rate.³¹ The scans are performed on a single

nanomagnet under ambient conditions, without feedback and hovering at a fixed height above the substrate. The spin resonance frequencies ν_{res}^{\pm} , in the relevant experimental configuration, read

$$\nu_{\text{res}}^{\pm} \simeq |\nu_0 \pm \gamma_{\text{NV}} B_{\text{NV}}|. \quad (1)$$

Here, $\nu_0 \simeq 2.87$ GHz is the ground state zero-field splitting parameter, and the total magnetic field is defined as $B_{\text{NV}} = \mathbf{B}_{\text{nm}} \cdot \hat{\mathbf{n}}_{\text{NV}} + B_{\text{bias}}$, where $\hat{\mathbf{n}}_{\text{NV}}$ is the spin quantization axis direction, and the bias field is assumed to be aligned to the spin axis. We are neglecting the local off-axis strain field contribution to the energy levels, and we assume to operate the system in the regime where $B_{\perp} \ll |\nu_0/\gamma_{\text{NV}} - |B_{\text{NV}}||$, where B_{\perp} is the magnitude of the field component orthogonal to the spin quantization axis.

All acquired scanned maps display stray field patterns consistent with a magnetic dipole field as confirmed by the dipole model fits shown in Fig. 2(a).

Approximating the nanomagnet as a dipole, we can extract the magnitude of the magnetic dipole moment m_{dip} from the dipole model fits (see [supplementary material S2](#)). We acquire a set of four scanned maps at different scanning heights to capture the stray field distribution at multiple distances from the nanomagnet. We increment the heights from 960 to 1460 nm above the nanomagnet in steps of $z_{\text{step}} = 166(5)$ nm. The maps of a set share the same experimental conditions otherwise. A simultaneous fit across all four scanned maps as shown in Fig. 2(b), incorporating the known height steps z_{step} , additionally constrains the fit parameters $r_{z,0}$ (depth of the approximated point-like dipole within the nanomagnet) and m_{dip} , which, for individual maps, can float in a correlated manner. The fit then allows quantitative inference of the magnetic moment magnitude m_{dip} . We repeat this fit procedure for external bias fields B_{bias} between 30 and 140 mT and plot $m_{\text{dip}}(B_{\text{bias}})$ in Figs. 2(c) and 2(d) (green stars). The estimated dipole moment magnitude $m_{\text{dip}}(B_{\text{bias}})$ increases linearly, indicating a soft magnetic nature of the FEBID-grown nanomagnet as expected from its typically amorphous structure.³²

For comparison, we similarly perform the simultaneous fits on stray field maps generated by a simulation of the nanomagnet, which is based on the dipole fit and AFM topography (see [supplementary material S3](#)), extracting $m_{\text{dip}}^{\text{sim}}(B_{\text{bias}})$ [red circles in Figs. 2(c) and 2(d)]

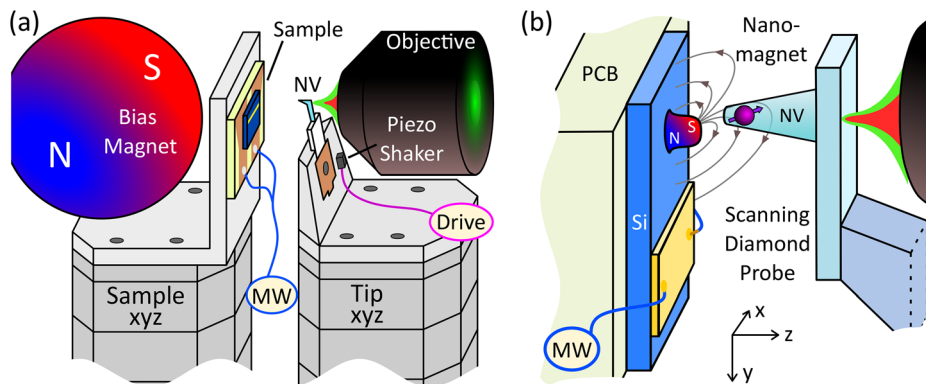


FIG. 1. Schematic of the scanning setup. (a) Sample and NV probe are mounted on two x , y , z piezo scanners. The nanomagnets are magnetized by a 4 cm-diameter spherical permanent magnet at a distance of a few millimeters. A 0.9 NA and 1 mm working distance objective focuses the collimated excitation beam onto the NV attached to a quartz tuning fork. A piezo shaker mechanically excites the tuning fork motion. (b) A single nanomagnet in proximity of the microwave (MW) stripline and the NV probe in the laboratory frame. The silicon chip is placed in the apparatus with a printed circuit board holder that also provides the microwave contacts.

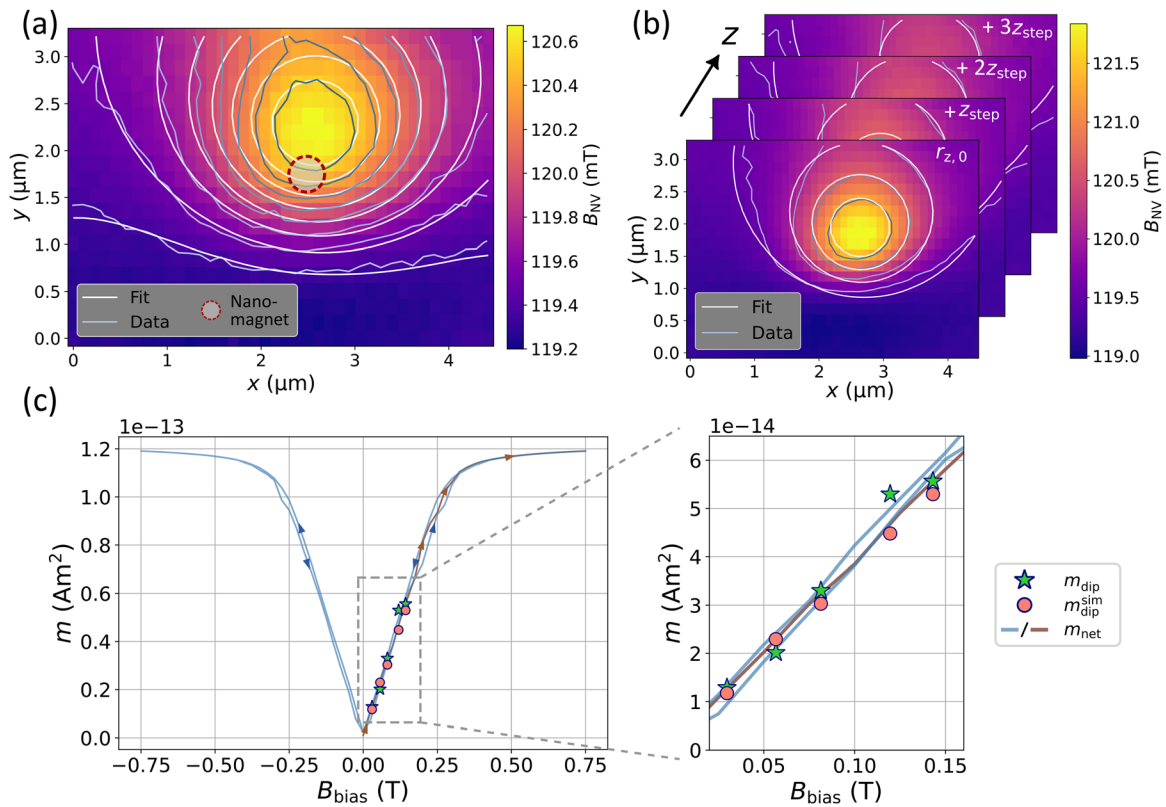


FIG. 2. Dipole fitting and stray field characterization. (a) A map of the measured B_{NV} at an estimated height of $h = 1294(40)$ nm above the nanomagnet and with $B_{bias} \sim 120$ mT. The white contour lines from a dipole model fit agree with the gray data contour lines of equal value. The indicated nanomagnet is centered around the dipole (x, y) position. (b) Simultaneous dipole fitting of four stray-field maps acquired at successive heights above the sample in increments of $z_{step} = 166(5)$ nm. A global dipole depth $r_{z,0}$ is enforced across all maps, while the relative height offset is fixed by the known step size. (c) Plot of the fitted dipole magnetic moment m_{dip} (green stars), dipole fitted m_{dip}^{sim} (red dots), and simulated net magnetization m_{net} (blue and brown lines) with increasing external biasing field. For the hysteresis curve of m_{net} , the external field is varied from $0 \text{ mT} \rightarrow 750 \text{ mT} \rightarrow -750 \text{ mT} \rightarrow 750 \text{ mT}$ in increments of 25 mT. The brown line marks the initial upswing from 0 to 750 mT, while the blue line corresponds to the remainder of the sweep. Arrows on the lines indicate the sweep direction of the external field. The inset displays a zoomed-in section of the boxed data region for improved visibility of the individual points.

that agrees well with $m_{dip}(B_{bias})$. Furthermore, we can calculate the net magnetic moment magnitude of the simulated nanomagnet via the volume integral of the magnetization $m_{net} \approx |\sum_{ijk} \mathbf{M}_{ijk} \Delta V|$, where \mathbf{M}_{ijk} is the magnetization in each simulation cell of volume ΔV . The moment magnitude $m_{net}(B_{bias})$ is depicted in Figs. 2(c) and 2(d). The agreement between m_{dip} , m_{dip}^{sim} , and m_{net} demonstrates mutual validation across of the experimental measurements, the dipole model fit, and the simulation.

The simulation of the magnetic structure predicts that the nanomagnet—that is $m_{dip}(B_{bias})$ —approaches saturation³³ at around $B_{bias} \sim 300$ mT. Supporting this prediction, we find agreement between the ratio of the bias fields $140 \text{ mT}/300 \text{ mT} = 0.47$ and the magnetization ratio $M/M_{sat} = 0.45$, where $M = m_{dip}(B_{bias} = 140 \text{ mT})/V$ with the nanomagnet volume V and saturation magnetization $M_{sat} = 1.26 \text{ MA m}^{-1}$ used for the simulation.³⁴

Foreseeing a future implementation of the experiment in which the magnetic structure is deposited on a high- Q resonator,³⁵ enabling coupling between the out-of-plane motion and the NV center, we are interested in a direct measurement of the magnetic gradient along the z -axis.

Under the applied B_{bias} , we measured the gradient G_z directly by the Zeeman shift from ODMR spectra as the NV center was scanned through the stray field near the nanomagnet. Guided by both the dipole model fit and the simulation, we identified the region of highest projected field gradient G_z while minimizing the magnetic field B_{\perp} that is transverse to $\hat{\mathbf{n}}_{NV}$, ensuring that the conditions of the Eq. (1) remain valid.

As shown in Figs. 3(a)–3(c), we find this region—which is governed by the relative angles between NV and magnetic dipole orientation—toward the edge of the nanomagnet. There, we approached the nanomagnet in the z direction and acquired ODMR spectra of the lower energy spin resonance at multiple positions to extract the projected magnetic field $B_{NV}(z)$ as a function of distance to the nanomagnet surface Δz .

In Fig. 3(d), we present the measured stray fields $B_{NV}(z)$ for the two approach trajectories exhibiting the highest field gradients, recorded at a bias field $B_{bias} \sim 120$ mT. The corresponding field gradients $G_z(z)$ are shown in Fig. 3(e), with maximum measured values of $B_{NV} = 40 \text{ mT} + B_{bias}$ and $G_z = 170 \text{ kT m}^{-1}$ obtained ~ 250 nm above the nanomagnet. Acquiring ODMR spectra closer to the surface

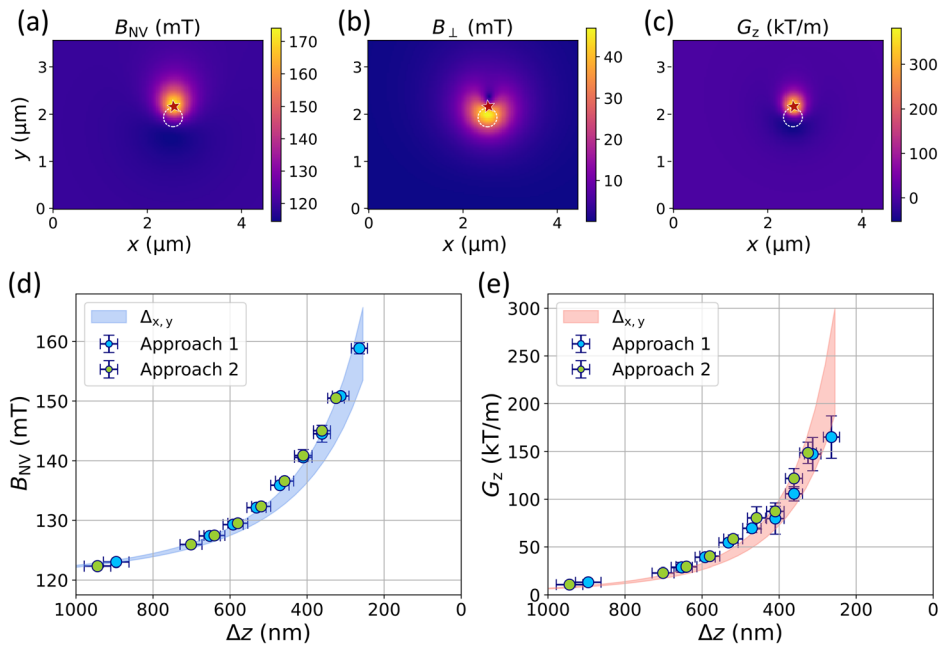


FIG. 3. Optimal approach region obtained from simulations for measuring the vertical gradient. (a)–(c) Simulation maps of B_{NV} , B_{\perp} , and G_z with the same x - and y -axes as Fig. 2(a) but at a height $h = 200$ nm above the nanomagnet. The white dotted circles mark the position and width of the simulated nanomagnet, and the red star highlights the approach location. (d) Plots of the measured magnetic field $B_{NV}(z) + B_{bias}$ and (e) the gradient $G_z(z)$ from two approaches as a function of the distance to the nanomagnet Δz . The zero points on the abscissa mark the AFM contact with the surface, which was measured before each approach. $\Delta_x = 111$ nm and $\Delta_y = 108$ nm correspond to the width of the vertically approached region. A description of the error bars is in supplementary material S4.

is hindered by the reduced ODMR signal contrast, which lowers the signal-to-noise ratio below unity (see supplementary material S4). We attribute this to mechanical drifts in the setup in the high-gradient field, primarily caused by microwave-induced heating.

After characterizing the DC behavior of the spin-mechanical system, we study the dynamics of the NV center using coherent spin control. We measured the spin decay time under spin-echo sequence, T_{2E} , while the NV probe was positioned above the nanomagnet [Fig. 4(a)]. The π -pulse time was first characterized with a Rabi measurement, from which we extract the π -pulse durations of ~ 55 ns. The spin-echo scheme shown in the inset of Fig. 4(a) was applied in two different

variations, where the rotation axis of the final $\pi/2$ -pulse is either along the X or the $-X$ axis as defined in the Bloch sphere in the inset of Fig. 4(b). Defining I_X and I_{-X} as the measured photoluminescence rate at the end of a spin-echo sequence for the two readout configurations, we compute the visibility $V_{echo} = (I_X - I_{-X}) / (I_X + I_{-X})$, which rejects the common-mode noise.³⁶ The visibility V_{echo} is then fitted with an exponential decay to extract T_{2E} . This measurement was repeated at different positions in the gradient field G_z . In Fig. 4(b), the dependency of T_{2E} on G_z is shown. The shift due to instabilities during T_{2E} measurements is indicated by horizontal error bars. Applying a MW drive causes thermal expansion of the substrate. The resulting change of the NV-surface distance produces a larger NV frequency shift at smaller distances due to the increased G_z . Therefore, it is not possible to apply accurate on-resonance pulses at gradients higher than 30 kT m^{-1} . The vertical error bars are extracted from the fit of T_{2E} .

Starting from a value $T_{2E} = 56(6) \mu\text{s}$ for a measurement far away from the nanomagnet, T_{2E} in Fig. 4(b) shows a significant decrease in value toward higher gradients. This trend can be attributed to either magnetic field noise from the magnetic nanostructure or thermal drifts of the system, which translates into fluctuations in the frequency of the NV center causing dephasing.²⁵ The nanomagnet's noise might be reduced by fully magnetizing the structure.

To show that the presented setup is suitable for performing a spin-mechanical experiment, we further measure the effect of the tuning fork mechanical oscillation on the spin dynamics. As the tuning fork is driven at its resonance frequency and vibrates along the x direction, we measure a series of unsynchronized spin-echo sequences (Fig. 5) with the NV center moving in a gradient $G_x = \partial B_{NV} / \partial x \simeq 540 \text{ T m}^{-1}$.

When the tuning fork is not driven, we see undisturbed decay of the visibility with a $T_{2E} = 42(3) \mu\text{s}$ (blue curve). In contrast to that, a driven tuning fork results in a modulated decay (red and green curves). It can be fitted to a zeroth order Bessel function,¹⁸

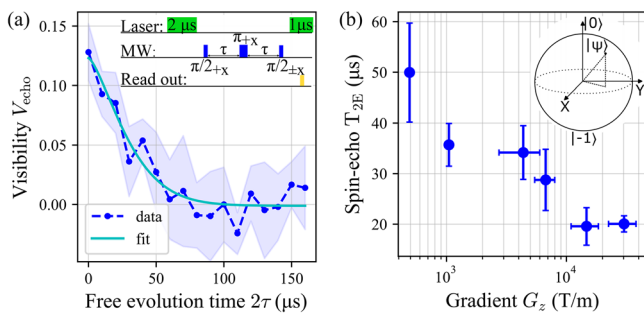


FIG. 4. Controlling the NV center's spin in a gradient field. (a) T_{2E} measurement in the gradient field of the nanomagnet. The inset shows the used pulse scheme. Visibility is calculated following Ref. 36 from two separate spin-echo measurements where the last $\pi/2$ pulse is either applied along the $+X$ or $-X$ axis. This measurement was done at $G_z = 4.4(1.6) \text{ kT m}^{-1}$ and gives $T_{2E} = 34.0(5.3) \mu\text{s}$. The shaded area shows the standard deviation. (b) Multiple T_{2E} measurements at different positions in the gradient field G_z of a nanomagnet. The measurements were done at distances between approximately 1587 and 540 nm. The Bloch sphere in the inset defines the axis of the rotation.

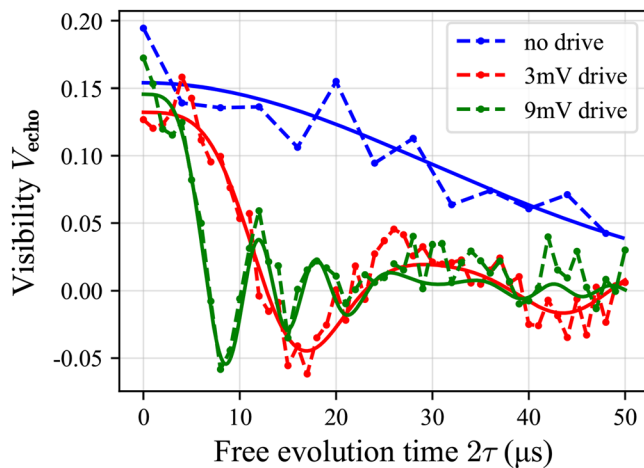


FIG. 5. Impact of mechanical oscillation of the tuning fork on the NV center. Blue curve shows a spin-echo measurement for an undriven tuning fork. The red and green curves show the measurement with a driven tuning fork at $\Omega_m \approx 32$ kHz with 3 and 9 mV driving amplitude, respectively. Data (dotted lines) can be fitted with a Bessel function of 0th order (full lines).

$$V_{\text{echo}} = \frac{C_{\text{NV}} J_0 \left(\frac{4\pi \gamma_{\text{NV}} x_0 G_x}{\Omega_m} (\cos(\Omega_m \tau) - 1) \right)}{2 - C_{\text{NV}}} \exp \left[- \left(\frac{2\tau}{T_{2E}} \right)^n \right], \quad (2)$$

clearly indicating spin-mechanical coupling, where C_{NV} is the contrast of our measurement and x_0 is the motional amplitude of the NV center (see [supplementary material S5.2](#)). In [Fig. 5](#), the exponent n is fixed to the average value $n = 2$, as extracted from the noise characterization in [Fig. 4\(b\)](#).

The oscillation amplitude values extracted from the fit are $x_0 = 3(1)$ nm (red curve) for a piezo drive amplitude of the tuning fork of 3 mV and $x_0 = 11(1)$ nm (green curve) for a drive amplitude of 9 mV. In the two configurations, the mechanical motion maps into an oscillating magnetic field with amplitude $2.0(6)$ μT and $6.1(8)$ μT at the position of the NV center.

In conclusion, we have demonstrated the generation of strong magnetic field gradients—up to 170 kT m^{-1} —using a soft cobalt nanostructure integrated into a spin-mechanics platform based on a scanning NV microscopy configuration. Spin coherence measurements performed in magnetic field gradients up to 25 kT m^{-1} revealed a coherence time T_{2E} of at least 20 μs . Considering that the experiments were conducted under open-loop mechanical conditions, we expect that, with cryogenic operation and active stabilization, spin manipulation at even higher field gradients could be achievable. Moreover, we observed a clear influence of the tuning fork motion on the NV spin coherence, indicating the presence of measurable spin-mechanical coupling in our setup.

Crucially, the noninvasive nature of the nanomagnet deposition via FEBID allowed us to decorate a silicon nitride membrane³⁷ with the magnetic structure (see [supplementary material S1.2](#)). This opens the path for further studies, including the investigation of potential changes in the mechanical quality factor resulting from the deposition—an essential step for future quantum spin-mechanics applications. If the membrane’s degradation is negligible, we consider a typical resonance frequency of 1.5 MHz, an effective mass of 2 ng, and

an ultra-high-quality factor³⁸ $Q = 10^9$ at 4 K, and then, with a spin coherence time of 1 ms (achievable by utilizing dynamical decoupling sequences³⁶) and a magnetic gradient of 170 kT m^{-1} , we obtain a single-phonon coupling strength $g_0/2\pi = 8$ Hz. This corresponds to a cooperativity $C = 5 \times 10^{-3}$, which is four orders of magnitude higher than current state-of-the-art setups.¹⁸

Remarkably, the force sensitivity of such a device—limited by the thermal contribution $S_{\text{th}} = 4k_B T m \Omega / Q = 4 \text{ aN}^2 / \text{Hz}$ (with k_B the Boltzmann constant)—would be comparable to the amplitude of the force produced by the oscillating spin $F = \mu_B G = 1.6$ aN, thus making it possible to detect the force exerted by the single spin within a few seconds averaging time, during which the spin can be re-polarized as necessary.

Reaching the milestone of $C \sim 1$ requires technical advances and appears feasible with the optimistic value³⁶ of $T_2 = 10$ ms and a gradient of 1 MT m^{-1} , predicted at a feasible distance of 150 nm from the magnetic structure at saturation.

Furthermore, the demonstrated ability to grow nanomagnets directly on membranes provides a promising platform for implementing quantum sensing experiments. While membranes have recently been integrated into scanning force microscopy setups^{39,40} and adopted in sample-on-resonator configurations for magnetic resonance force detection,⁴¹ we foresee their use in magnetic resonance force microscopy experiments in the practical “magnet-on-resonator” configuration⁴² as well as for advancing nanoscale magnetic resonance imaging techniques.¹⁰

Finally, the high degree of control offered by the FEBID technique enables the tailoring of nanomagnet geometry to suit specific experimental requirements of the magnetic field, making it a versatile tool for future developments in hybrid quantum systems.

See the [supplementary material](#) for additional details on the microwave and nanomagnet fabrication, nanomagnet simulation, experimental setup, and the structural analysis.

The authors thank Christian Degen for valuable feedback, Amalio Fernández-Pacheco and Naëmi Leo for providing early test samples, and Tim Turan for contributions to the experimental setup. F.H. and L.Ž. thank Kai Wagner, Matteo Tassarolo, and Patrick Maletinsky for fruitful discussions and the opportunity to perform early measurements on their NV setup. This work was supported by the European Research Council (ERC) under project PHOQS (Grant No. 101002179), the Novo Nordisk Foundation (Grant No. NNF20OC0061866), the Danish National Research Foundation through the Centre of Excellence “Hy-Q,” the Independent Research Fund Denmark (Grant No. 1026-00345B), and the Swiss National Science Foundation (Grant No. CRSII5 177198/1). L.S. acknowledges financial support from the European Union’s Horizon 2021 research and innovation programme under the Marie Skłodowska-Curie (Grant Agreement No. 101063285). L.Ž. and M.P. acknowledge financial support from the Swiss National Science Foundation (Grant No. 207933).

AUTHOR DECLARATIONS

Conflict of Interest

The authors have no conflicts to disclose.

Author Contributions

Felix Hahne, Teresa Klara Pfau, and Liza Žaper contributed equally to this work.

Felix Hahne: Formal analysis (equal); Investigation (lead); Methodology (equal); Visualization (equal); Writing – original draft (equal). **Teresa Klara Pfau:** Formal analysis (equal); Investigation (equal); Methodology (equal); Software (lead); Visualization (equal); Writing – original draft (equal). **Liza Žaper:** Investigation (equal); Methodology (equal); Resources (lead); Visualization (equal); Writing – original draft (equal). **Lucio Stefan:** Conceptualization (equal); Data curation (equal); Formal analysis (equal); Investigation (equal); Methodology (equal); Project administration (equal); Software (equal); Writing – review & editing (equal). **Thibault Capelle:** Resources (equal); Writing – review & editing (equal). **Andrea Ranfagni:** Formal analysis (equal); Investigation (equal); Methodology (equal); Supervision (equal); Visualization (equal); Writing – original draft (equal). **Martino Poggio:** Funding acquisition (equal); Project administration (equal); Supervision (equal); Writing – review & editing (equal). **Albert Schliesser:** Conceptualization (lead); Funding acquisition (equal); Project administration (equal); Supervision (equal); Writing – review & editing (equal).

DATA AVAILABILITY

The data that support the findings of this study are available from the corresponding author upon reasonable request.

REFERENCES

- D. Rugar, R. Budakian, H. J. Mamin, and B. W. Chui, *Nature* **430**, 329–332 (2004).
- M. D. LaHaye, J. Suh, P. M. Echternach, K. C. Schwab, and M. L. Roukes, *Nature* **459**, 960–964 (2009).
- A. D. O’Connell, M. Hofheinz, M. Ansmann, R. C. Bialczak, M. Lenander, E. Lucero, M. Neeley, D. Sank, H. Wang, M. Weides, J. Wenner, J. M. Martinis, and A. N. Cleland, *Nature* **464**, 697–703 (2010).
- J.-M. Pirkkalainen, S. U. Cho, J. Li, G. S. Paraoanu, P. J. Hakonen, and M. A. Sillanpää, *Nature* **494**, 211–215 (2013).
- S. Etaki, M. Poot, I. Mahboob, K. Onomitsu, H. Yamaguchi, and H. S. J. van der Zant, *Nat. Phys.* **4**, 785–788 (2008).
- M. Montinaro, G. Wüst, M. Munsch, Y. Fontana, E. Russo-Averchi, M. Heiss, A. Fontcuberta i Morral, R. J. Warburton, and M. Poggio, *Nano Lett.* **14**, 4454–4460 (2014).
- D. A. Golter, T. Oo, M. Amezcuca, K. A. Stewart, and H. Wang, *Phys. Rev. Lett.* **116**, 143602 (2016).
- A. Bachtold, J. Moser, and M. I. Dykman, *Rev. Mod. Phys.* **94**, 045005 (2022).
- U. L. Andersen, J. S. Neergaard-Nielsen, P. van Loock, and A. Furusawa, *Nat. Phys.* **11**, 713–719 (2015).
- A. Eichler, *Mater. Quantum Technol.* **2**, 043001 (2022).
- M. W. Doherty, N. B. Manson, P. Delaney, F. Jelezko, J. Wrachtrup, and L. C. Hollenberg, *Phys. Rep.* **528**, 1–45 (2013).
- A. Barfuss, J. Teissier, E. Neu, A. Nunnenkamp, and P. Maletinsky, *Nat. Phys.* **11**, 820–824 (2015).
- P. Overtchaiyapong, K. W. Lee, B. A. Myers, and A. C. B. Jayich, *Nat. Commun.* **5**, 4429 (2014).
- O. Arcizet, V. Jacques, A. Siria, P. Poncharal, P. Vincent, and S. Seidelin, *Nat. Phys.* **7**, 879–883 (2011).
- S. Kolkowitz, A. C. Bleszynski Jayich, Q. P. Unterreithmeier, S. D. Bennett, P. Rabl, J. Harris, and M. D. Lukin, *Science* **335**, 1603–1606 (2012).
- B. Pigeau, S. Rohr, L. Mercier de Lépinay, A. Gloppe, V. Jacques, and O. Arcizet, *Nat. Commun.* **6**, 8603 (2015).
- T. Oeckinghaus, S. A. Momenzadeh, P. Scheiger, T. Shalomyayeva, A. Finkler, D. Dasari, R. Stöhr, and J. Wrachtrup, *Nano Lett.* **20**, 463–469 (2020).
- F. Fung, E. Rosenfeld, J. D. Schaefer, A. Kabcenell, J. Gieseler, T. X. Zhou, T. Madhavan, N. Aslam, A. Yacoby, and M. D. Lukin, *Phys. Rev. Lett.* **132**, 263602 (2024).
- S. Hong, M. S. Grinolds, P. Maletinsky, R. L. Walsworth, M. D. Lukin, and A. Yacoby, *Nano Lett.* **12**, 3920–3924 (2012).
- J. Gieseler, A. Kabcenell, E. Rosenfeld, J. D. Schaefer, A. Safira, M. J. A. Schuetz, C. Gonzalez-Ballester, C. C. Rusconi, O. Romero-Isart, and M. D. Lukin, *Phys. Rev. Lett.* **124**, 163604 (2020).
- P. Rabl, P. Cappellaro, M. V. G. Dutt, L. Jiang, J. R. Maze, and M. D. Lukin, *Phys. Rev. B* **79**, 041302 (2009).
- S. D. Bennett, S. Kolkowitz, Q. P. Unterreithmeier, P. Rabl, A. C. Bleszynski Jayich, J. G. E. Harris, and M. D. Lukin, *New J. Phys.* **14**, 125004 (2012).
- P. Rabl, S. J. Kolkowitz, F. H. L. Koppens, J. G. E. Harris, P. Zoller, and M. D. Lukin, *Nat. Phys.* **6**, 602–608 (2010).
- E. Rosenfeld, R. Riedinger, J. Gieseler, M. Schuetz, and M. D. Lukin, *Phys. Rev. Lett.* **126**, 250505 (2021).
- D. Lee, K. W. Lee, J. V. Cady, P. Overtchaiyapong, and A. C. B. Jayich, *J. Opt.* **19**, 033001 (2017).
- M. De Teresa, A. Fernández-Pacheco, R. Córdoba, L. Serrano-Ramón, S. Sangiao, and M. R. Ibarra, *J. Phys. D: Appl. Phys.* **49**, 243003 (2016).
- QZabre Ltd., see <https://www.qzabre.com/> for “Qzabre Quantum Scanning Tips” (2025).
- G. Balasubramanian, I. Y. Chan, R. Kolesov, M. Al-Hmoud, J. Tisler, C. Shin, C. Kim, A. Wojcik, P. R. Hemmer, A. Krueger, T. Hanke, A. Leitenstorfer, R. Bratschkitsch, F. Jelezko, and J. Wrachtrup, *Nature* **455**, 648–651 (2008).
- P. Maletinsky, S. Hong, M. S. Grinolds, B. Hausmann, M. D. Lukin, R. L. Walsworth, M. Loncar, and A. Yacoby, *Nat. Nanotechnol.* **7**, 320–324 (2012).
- L. Rondin, J.-P. Tetienne, T. Hingant, J.-F. Roch, P. Maletinsky, and V. Jacques, *Rep. Prog. Phys.* **77**, 056503 (2014).
- A. Gruber, A. Dräbenstedt, C. Tietz, L. Fleury, J. Wrachtrup, and C. v Borczyskowski, *Science* **276**, 2012–2014 (1997).
- A. Fernández-Pacheco, L. Skoric, J. M. De Teresa, J. Pablo-Navarro, M. Huth, and O. V. Dobrovolskiy, *Materials* **13**, 3774 (2020).
- J. M. Coey, *Magnetism and Magnetic Materials* (Cambridge University Press, 2010).
- L. Žaper, P. Rickhaus, M. Wyss, B. Gross, K. Wagner, M. Poggio, and F. Braakman, *ACS Appl. Nano Mater.* **7**, 3854–3860 (2024).
- Y. Tsaturyan, A. Barg, E. S. Polzik, and A. Schliesser, *Nat. Nanotechnol.* **12**, 776–783 (2017).
- N. Bar-Gill, L. M. Pham, A. Jarmola, D. Budker, and R. L. Walsworth, *Nat. Commun.* **4**, 1743 (2013).
- L. Catalini, Y. Tsaturyan, and A. Schliesser, *Phys. Rev. Appl.* **14**, 014041 (2020).
- M. Rossi, D. Mason, J. Chen, Y. Tsaturyan, and A. Schliesser, *Nature* **563**, 53–58 (2018).
- D. Hälgl, T. Gislser, Y. Tsaturyan, L. Catalini, U. Grob, M.-D. Krass, M. Héritier, H. Mattiat, A.-K. Thamm, R. Schirhagl, E. C. Langman, A. Schliesser, C. L. Degen, and A. Eichler, *Phys. Rev. Appl.* **15**, L021001 (2021).
- T. Gislser, D. Hälgl, V. Dumont, S. Misra, L. Catalini, E. C. Langman, A. Schliesser, C. L. Degen, and A. Eichler, *Phys. Rev. Appl.* **22**, 044001 (2024).
- N. Scozzaro, W. Ruchotzke, A. Belding, J. Cardellino, E. C. Blomberg, B. A. McCullian, V. P. Bhallamudi, D. V. Pelekhov, and P. C. Hammel, *J. Magn. Reson.* **271**, 15–20 (2016).
- G. Longenecker, H. J. Mamin, A. W. Senko, L. Chen, C. T. Rettner, D. Rugar, and J. A. Marohn, *ACS Nano* **6**, 9637–9645 (2012).